Additive manufacturing of lattice electrodes for electrocatalyst discovery

Robert Ortmann[1] · Olga A. Krysiak[2] · Nick Hantke[1] · Negar Sangtarash[2] · Tobias Grimm[1] · Jan T. Sehrt[1]

1 Chair of Hybrid Additive Manufacturing, Ruhr-Universität Bochum, Universitätsstraße 150, 44801 Bochum, Germany

2 xemX materials space exploration GmbH, Semperstrasse 113, 44801 Bochum, Germany

Abstract

Large-scale production of green hydrogen and the transition of industrial processes to its use is one of the major challenges of industrial decarbonisation. Due to the use of rare and noble metals in the production of electrocatalysts, large-scale production is often uneconomical and the development of new electrocatalysts inevitable. Since the activity of an electrocatalyst depends on the materials used and the number of active sites, lattice structures and metallic foams as electrode substrates as well as coatings with small particles have proven to be feasible approaches for increasing the output performance. Besides, the replacement of noble metal catalysts with multi-elemental catalysts, for example, high entropy alloys, offers the possibility of providing a variety of different active sites to achieve high material activity at lower cost.

In this study, powder bed fusion of metals using a laser beam is used to manufacture lattice structures of different sizes from NiCr19Fe19Nb5Mo3 (Inconel® Alloy 718). High surface-to-volume ratios are achieved using an exposure strategy specifically adapted to produce lattice structures. Overpotentials for the oxygen and hydrogen evolution reactions of fabricated lattices are determined using a laboratory-scale water electrolyser. Additionally, performance measurements of lattice structures coated with various electrocatalyst materials are performed. The results show a dependency between the overpotential and the geometry and the process parameters used for the additive manufacturing of the uncoated lattice structures. Coated lattices show increased activity depending on the coating material, cavity size and volume.

Keywords   Additive manufacturing · Powder Bed Fusion of Metals using a Laser Beam · Lattice · Multi-metal electrocatalysts · Electrocatalysis · Oxygen Evolution Reaction · Hydrogen Evolution Reaction

1. Introduction

Hydrogen and hydrogen-based fuels are a pillar of the transition towards a world with net-zero carbon emissions [1]. In particular, industrial processes and transport, which account for about 60 % of the total CO_2 emissions [2] are facing the need for decarbonisation from fossil fuels to renewable energy sources. Electrification is seen as a possible solution to date, but the diverse use of fossil fuels makes it difficult to decarbonise all processes through electrification alone [3, 4]. For the remaining processes, the use of green hydrogen as an energy carrier is seen as a possible solution, as it enables the storage and supply of large amounts of energy [4], even across the seasons [3, 5]. Water electrolysis, also known as water splitting, is a possibility for the production of green hydrogen, assuming that renewable energies are used in the process [3]. Here, electricity separates water into its constituent elements through two distinct electrochemical reactions at separate electrodes. Hydrogen is produced at the cathode in the hydrogen evolution reaction (HER) and oxygen at the anode in the oxygen evolution reaction (OER). However, since rare and noble metals are used in the electrocatalysts, scaling up these processes is often not economical and has led to extensive research in the field of electrocatalyst discovery [6].

Additive manufacturing (AM), and especially powder bed fusion of metals using a laser beam (PBF-LB/M according to [7]), has proven to be a suitable manufacturing process for the rapid production of components with specific mechanical and technological properties [8]. In the PBF-LB/M process, a powder feedstock material is raked onto a build platform or a previously manufactured layer and is locally and selectively melted by a laser beam to produce a bonding between adjacent laser tracks and the subsequently manufactured layers during solidification [9]. The design freedom of PBF-LB/M enables the production of lattice structures, which have a large surface area per volume and weight [10] and are thus suitable for the

production of catalysts substrates or catalysts themselves.

Lattice structures are used in AM for a variety of applications and purposes, such as weight reduction [11], time and cost saving [11], waste reduction [12, 13], manufacturing of energy absorbers [11, 14], structures with high stiffness-to-weight-ratio, low elastic modulus or large specific surface area [10]. Due to the versatile properties and the fact that the structures are formed by a repetitive spatial arrangement of specific unit cells [11, 14, 15], nearly freely configurable geometries according to AM constraints [16] can be produced, fulfilling the requirements of various industries such as medical [11, 17], automotive [11, 14] and aerospace [11, 18].

Current research in the field of AM of components for use in electrocatalysis is mostly focused on the processing of electrocatalytic materials or on the exploitation of design freedom for the optimisation of the design of water splitting electrolyser cells [19]. Different AM methods according to DIN EN ISO/ASTM 52900 [7] are utilized for the manufacturing of electrocatalysts or electrodes for subsequent coating, such as Material Extrusion [13, 20–25], Vat Photopolymerization [26, 27] and Powder Bed Fusion [28–31]. In Powder Bed Fusion, investigated materials include stainless steel 316L [28, 29, 32, 33], Ti6Al4V [30] and high entropy alloys [34]. For high entropy alloys transition metals and their sulphides and phosphides are seen as potential materials [19].

The research on new electrocatalysts has been characterised by increasing interest in materials containing more than one chemical element in the last couple of years. This trend can be explained by the fact that it was proven before that mixing various elements with distinct electrochemical activities (also using those which are known as relatively poor catalysts) can lead to the creation of materials with high electrochemical activity. This is often comparable to the activity of noble metal electrocatalysts, but not containing any of them or containing only a limited amount of expensive and rare elements. [35, 36]

This phenomenon was previously explained by the synergistic interaction between elements and the formation of multiple active sites, which are unavailable for single elements and their simple combinations, allowing further tuning of the electrocatalytic activity. [37, 38]. The main problem associated with this approach is the lack of clear-cut rules and theoretical predictions, often being insufficient in terms of determining which elements to combine and in which molar ratio. Considering the number of available chemical elements in the periodic table, this leads to a vast option space and the necessity of conducting many experiments. To address this problem and limit the number of required tests, approaches like using machine learning or density functional theory (DFT) calculation in combination with high-throughput experimentation were successfully applied.

Numerous synthesis techniques were reported as suitable for the synthesis of multi-metal electrocatalysts. Many require high pressure and temperature: solvothermal [39, 40], hydrothermal synthesis [41], high-temperatures: thermal shock [42], arc-melting [43] or expensive equipment: laser deposition [44, 45], physical [46, 47] or chemical vapour deposition [48]. Electrodeposition [49] and spray-based synthesis [50, 51] methods are considered low-cost, suitable to produce significant amounts of material and easy to operate.

In this work, lattice structures of different sizes are manufactured from NiCr19Fe19Nb5Mo3 (Inconel® Alloy 718) using a novel spot-based exposure approach and used as electrodes (anodes and cathodes) for water electrolysis. Furthermore, polymer/metal precursor spraying synthesis [52] is used to coat such prepared electrodes with known and not yet reported electrocatalysts for both hydrogen and oxygen evolution reactions.

2. Materials and Methods

2.1. Additive manufacturing process

AM of lattices was performed using the PBF-LB/M system Aconity Midi (Aconity GmbH) equipped with a 400 W fibre laser source with a wavelength of 1070 nm. Argon shielding gas atmosphere was used at an oxygen content of < 100 ppm. Manufactured lattices consist of symmetric body-centred cubic (BCC) unit cells with a size of 250, 500, and 1000 μm and sample size of 1 mm x 10 mm (x-y) and a height of 10 mm (z) (Fig. 1).
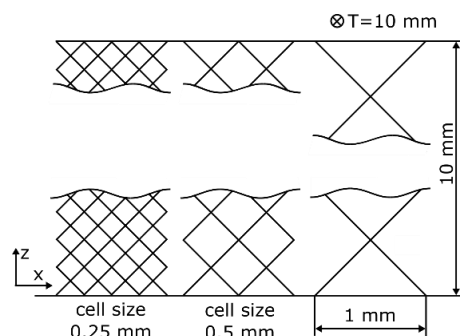

Figure 1: Schematic indicating size, orientation and arrangement of unit cells in manufactured samples

The exposure was carried out with a spot-based exposure approach. For this purpose, the centre-coordinates of the cross-section of each lattice-strut are calculated and, by synchronising the laser source and the scanner unit, melted sequentially point by point (Fig. 2). For the investigation of the influencing variables, based

on previous investigations on the processing window for bulk samples, a nominal laser power of 100, 150 and 200 W, a focal diameter of 80 µm and 120 µm, and an exposure time of 100 µs, 250 µs and 500 µs were used.
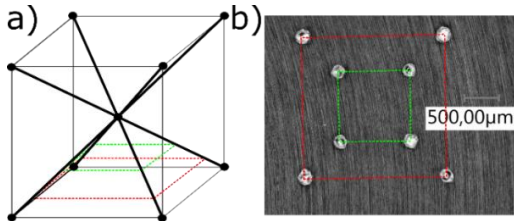

Figure 2:Body-centered cubic unit cell (a) and schematic representation of spot-based exposure strategy (b)

Gas-atomized powder feedstock material NiCr19Fe19Nb5Mo3 (Inconel® Alloy 718) was used for manufacturing of the lattice structures. The analysis of the powder feedstock morphology and samples was carried out using a SEM Gemini 2 (Carl Zeiss Microscopy Deutschland GmbH) and is shown in Fig. 3. The morphology is predominantly spherical, but non-spherical particles and splatters are also observed.
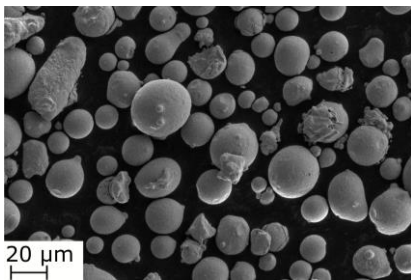

Figure 3: SEM image of the powder feedstock material NiCr19Fe19Nb5Mo3 used in this study at 500× magnification

The particle size distribution of the powder feedstock was measured using a Camsizer X2 (Microtrac Retsch GmbH) with a Xjet module and 150 kPa dispersion pressure and is shown in Fig. 4. The powder has a common particle size distribution used for PBF-LB/M ranging from 15 µm to about 53 µm and a d_{10} of 18.96 µm, d_{50} of 29.51 µm, and d_{90} of 43.19 µm.

Density of manufactured lattices was measured using Archimedes' principle utilizing isopropyl alcohol and analytical balance ALJ series (Carl Roth GmbH+Co. KG) with an accuracy of < 0.05 %. Relative density was then calculated using the material density of NiCr19Fe19Nb5Mo3 of 8.2 g·cm^{-3} [53]. The strut diameter analysis was performed using an optical microscope Keyence VHX-6000 series (Keyence Deutschland GmbH) at 300× magnification.

The surface of manufactured lattices and Ni-foam electrode material was measured using static-volumetric krypton adsorption technique (multipoint BET) with BELSORP MAX X 334 (Microtrac Retsch GmbH). The calculation of the sample surface was carried on condition of an adsorption energy input constant C > 0

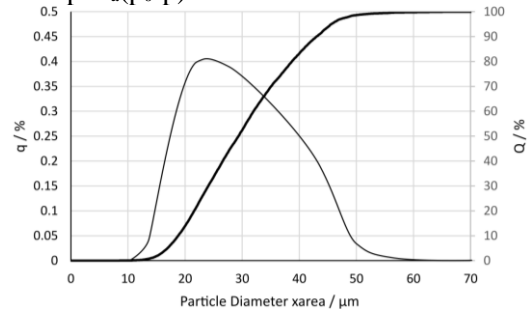and a correlation of relative pressure to pressure/volume ratio $p/V_a(p_0-p) > 0.99$.

Figure 4: Particle size distribution of the powder feedstock material NiCr19Fe19Nb5Mo3 used in this study

2.2. Coating

The coating of manufactured lattices was performed using a polymer/metal precursor spraying technique, as presented in [52]. A solution of metal precursors (nitrates and/or chlorides of coating feedstock elements) and polyvinylpyrrolidone (PVP) was sprayed onto the target kept at 120 °C (see Fig. 5), forming a polymer/metal matrix. For most of the metals, nitrates salts (Merck, purity at least > 99 %) were used (Ni, Fe, Co, Cr, Mn, Pd, Cu); for those when nitrate is not available, chloride form was used (Ru, Mo). A subsequent two-stage heat treatment process transformed the coating into a stable oxide layer. In the first step, a $10\%H_2/90\%Ar$ atmosphere at 800 °C was used to obtain the degradation of metal precursors and graphitisation of carbon. The stable oxide layer was then formed in the second step in a $10\%O_2/90\%Ar$ atmosphere at 250 °C. [52]

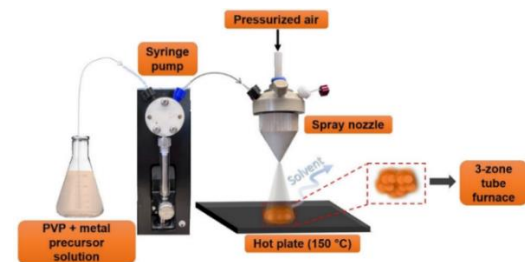*Figure 5: Schematic illustration of polymer/metal precursor spraying synthesis process [52]. Temperature was changed to 120 °C in this study*

Coating quality assurance was performed using SEM and SEM-EDX imaging with a JEOL JSM-7200F operating at a working distance of 10 mm and with an accelerating voltage of 30 kV.

2.3. Electrocatalysis experiments

Prepared lattice electrodes, as well as lattice electrodes coated with electrocatalyst, were incorporated as cathode (evaluating activity towards hydrogen evolution) or anode (evaluating activity towards oxygen

evolution reaction) into a self-build 2-compartment flow-through electrolysis cell. The activity and short-term stability (1 h) during alkaline water electrolysis were assessed in a 3-electrode system. The working electrode was always a lattice electrode (coated or not), the counter electrode was Ni mesh (Goodfellow), and the reference electrode was a double junction (1 M KOH) Ag/AgCl/3 M KCl electrode. The reference electrode was kept at a fixed distance from the working electrode. The gasket opening determined the geometrical surface area of the working and counter electrode to be 0.95 cm^2. Electrolyte, 1 M KOH (86.4 %, Fisher Scientific) prepared in ultrapure water, was purified with Chelex 100 cation-exchange resin (Sigma-Aldrich) before use. During the measurement, the electrolyte was constantly flowing, in separate flows, through each compartment of the electrolysis cell due to using a peristaltic pump. Measurements were conducted using the potentiostat/galvanostat Autolab PGSTAT128 N (Metrohm). First, electrochemical impedance spectroscopy (EIS) in galvanostatic mode at 0 mA, in a frequency range between 100 kHz and 10 Hz, was conducted to assess the value of uncompensated resistance. After it, one linear sweep voltammogram (LSV) (from 90 mV to 70 mV vs RHE) was recorded, followed by chronopotentiometry (CP) measurement at -50 mA·m^{-2} for 1 h and another LSV.

All potentials are reported versus reversible hydrogen electrode (RHE) and were calculated according to the equation:

$$U_{RHE}(V) = U_{Ag|AgCl|3\,M\,KCl}(V) + 0.210\,(V) + (0.059 \cdot pH)$$

Where $U_{Ag/AgCl/3\,M\,KCl}$ is potential versus Ag/AgCl/3 M KCl electrode, 0.210 V is the standard potential of Ag/AgCl/3 M KCl reference electrode at 25 °C, 0.059 is the result of Nernst equation at 25 °C and pH value of the electrolyte is 14.

3. Results and Discussion

The cell size of the unit cells, the laser power, the exposure time and the focus diameter were investigated as central influencing variables for the generation of electrodes with large surfaces for subsequent coating. Fig. 6 shows samples with unit cell sizes of 250 μm (a), 500 μm (b) and 1000 μm (c). Due to the reduced pore size and volume, the manufacturing of samples with smaller unit cell sizes enables the realisation of a larger surface area per volume. However, the probability of the struts joining to form a closed surface and the disappearance of the pores increases for samples manufactured with higher energy input.

The energy applied to the cross-sectional area is determined by the laser power and the exposure time. The influence of the laser power on the geometry of the lattice struts is depicted in Figure 7. An increasing strut

diameter and the adhesion of powder particles to the downward-facing surfaces of struts is observed for increasing laser powers from 100 W (Fig. 7, a), to 150 W (Fig. 7, b) and 200 W (Fig. 7, c) respectively.
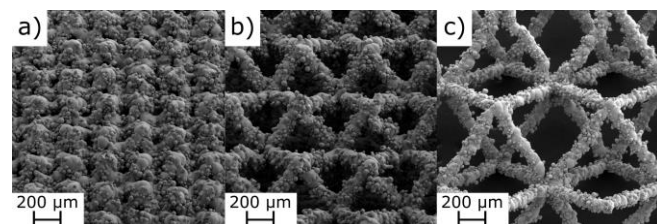

Figure 6: SEM images of lattices with a cell size of 250 μm (a), 500 μm (b) and 1000 μm (c) manufactured with a laser power of 100 W, exposure time of 100 μs and a focal diameter of 80 μm at 50× magnification acquired using Zeiss Gemini2 at an angle of 30°
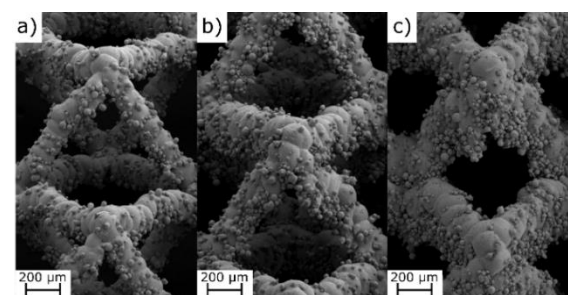

Figure 7: SEM images of lattices with a cell size of 1000 μm manufactured with laser powers of 100 W (a), 150 W (b) and 200 W (c), exposure time of 250 μs and a focus diameter of 80 μm at 50× magnification acquired using Zeiss Gemini2 at an angle of 30°

The increased strut diameter is also linked to a reduced pore size and volume and is similarly observed with the increase of energy input through an increased exposure time at constant power (see Fig. 8). However, no significant additional adhesion of powder particles to the downward-facing surfaces is observed for increased exposure times from 100 μs (Fig. 8, a) to 250 μs (Fig. 8, b) and 500 μs (Fig. 8, c) respectively.
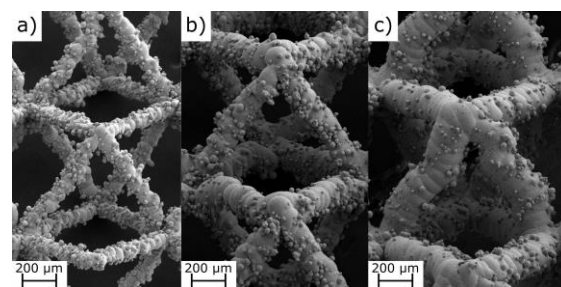

Figure 8: SEM images of lattices with a cell size of 1000 μm manufactured with a laser power of 100 W, exposure time of 100 μs (a), 250 μs (b) and 500 μs (c) and a focus diameter of 80 μm at 50× magnification acquired using Zeiss Gemini2 at an angle of 30°

For the variation of the focus diameter (see Fig. 9), a reduction of the strut diameter is observed upon increasing the focus diameter from 80 μm (a) to 120 μm (b). In addition, a reduced number of powder

adhesions are observed on the manufactured structures, possibly resulting from a reduced thermal gradient due to the reduced energy density of the laser beam with an increased focus diameter. With regard to the application, however, the adhesion of the powder particles to the manufactured structures is considered beneficial, as it results in a higher surface-to-volume ratio.
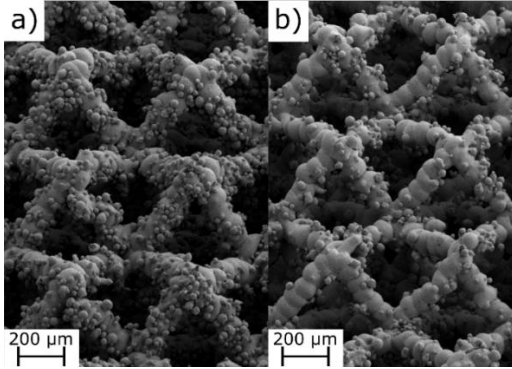

Figure 9: SEM images of lattices with a cell size of 500 μm manufactured with a laser power of 100 W, exposure time of 100 μs and a focus diameter of 80 μm (a) and 120 μm (b) at 50× magnification acquired using Zeiss Gemini2 at an angle of 30°

The previously shown qualitative influence of the processing parameters on the strut diameter is also investigated quantitatively and shown in Figure 10. The minimum mean strut diameter of 69.6 μm was achieved with the lowest laser power of 100 W, exposure time of 100 μs and a focus diameter of 120 μm. In contrast, a strut diameter of up to 304 μm was measured for the highest energy inputs used. It can also be observed that for cells with a unit cell size of 250 μm and 500 μm, depending on the process parameters, a closed structure rather than a lattice structure is manufactured due to the struts combining and filling the pore volumes of the lattice structure. In this application, this is considered disadvantageous as it leads to inaccessibility of the inner surface of the lattice structure and reduces the coatability. The unit cell size of 250 μm was therefore not considered for the coating procedure. Furthermore, at identical process parameters, an increased strut diameter is observed for lattices with larger unit cell sizes. This is possibly due to the interaction of the surrounding powder with the melt pool. Possibly due to the previously manufactured struts close to the laser-powder interaction zone, there is less loose and more solidified powder in the surroundings of the melt pool, resulting in an increased heat dissipation capacity of the environment and a lower probability of further loose powder particles entering the melt pool.

The stability of the manufactured struts, which is required for installation between sealings in the electrolyser cell setup, was estimated using the volumetric density determined using Archimedes' principle (Table 1). The highest mean density for the lattices with a unit cell size of 500 μm was obtained using an exposure time of 100 μs. For a cell size of 1000 μm, the highest arithmetic density was obtained using an exposure time of 250 μs. Both sets of parameters were therefore taken into account for the coating experiments. Based on the investigations regarding the powder particle adhesion to the lattice structures, a laser focus diameter of 80 μm was also selected for further electrode production, the coating process and the electrocatalytic experiments.

Table 1: Relative density of manufactured lattice structures measured using Archimedes' principle

Cell Size = 250 μm						
Laser Power	100 W		150 W		200 W	
Focus Diameter / Exposure time	80 μm	120 μm	80 μm	120 μm	80 μm	120 μm
100 μs	0.957	0.974	0.896	0.988	0.867	0.938
250 μs	0.904	0.952	0.939	0.941	0.952	0.945
500 μs	0.968	0.929	0.986	0.995	0.941	0.904
Cell Size = 500 μm						
Laser Power	100 W		150 W		200 W	
Focus Diameter / Exposure time	80 μm	120 μm	80 μm	120 μm	80 μm	120 μm
100 μs	0.999	0.997	0.997	0.998	0.956	0.995
250 μs	0.992	0.996	0.928	0.994	0.868	0.957
500 μs	0.993	0.995	0.973	0.994	0.899	0.965
Cell Size = 1000 μm						
Laser Power	100 W		150 W		200 W	
Focus Diameter / Exposure time	80 μm	120 μm	80 μm	120 μm	80 μm	120 μm
100 μs	0.955	0.970	0.966	0.987	0.967	0.966
250 μs	0.977	0.980	0.999	0.995	0.982	0.999
500 μs	0.997	0.965	0.995	0.984	0.972	0.979

Several factors influence the performance of an electrode used for water electrolysis, broadly categorized into material properties, design considerations, and operating conditions [18, 19, 30, 34, 61, 62]. Within the material properties group, factors such as catalyst material, conductivity and surface area are included. Operating conditions are mainly the choice of electrolyte, temperature, pressure, electrolyte flow rates or operating current density. The last group, design consideration, is the most interesting in the context of additive manufacturing, as it can be easily customized with this technology. The design and structure of the electrode can impact performance. Porous electrodes or nanostructured materials can enhance the surface area and promote better electrolyte contact, essential for efficient electrolysis. Better electrolyte contact is achieved by removing the gas bubbles formed during the reaction from the electrode surface more efficiently, which is due to the pore size, distribution and affinity of the electrode material to the reaction products. Taking this factor into consideration, the set of six types of lattice structures (cell size 500 and 1000 μm manufactured with varying laser power 100, 150, and 200 W) were then used as electrodes for OER and HER in water electrolysis in the flow-through cell. The first
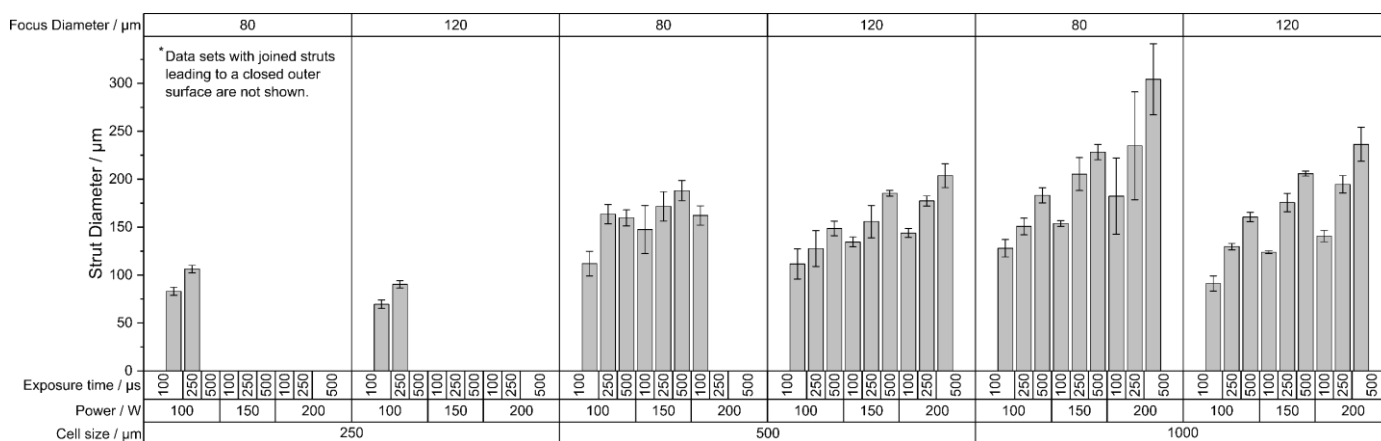
Figure 10: Measured strut diameters of the lattice structures as a function of unit cell size and processing parameters laser power, exposure time and focus diameter measured using Keyence VHX-6000 series

two electrodes of each type were measured as-built, one as anode with Ni foam as cathode and the second as cathode with Ni foam as anode. Figure 11 presents a comparison of chronopotentiometry (CP) curves recorded for all types of lattice electrodes used as cathodes (a) and anodes (b). For cathode measurements, it is visible that most of the samples exhibit very similar performance, with the overpotential for HER at -50 mV·cm^{-2} being between 460 and 500 mV. An exception are two samples that were produced with the parameters that differ most from each other. An electrode with a cell size of 500 µm prepared with 200 W laser power is the densest electrode, and an electrode with a cell size of 1000 µm and 100 W laser power is the most open. The performance of the close-packed electrode was the best for HER, that of the most open electrode the worst. Additionally, all tested electrodes are stable during the 1 h electrolysis experiment (change of the measured potential value is negligible). In the case of testing uncoated electrodes for OER, the trend is a bit different. All electrodes with 500 µm cell size perform alike (overpotential at 50 mA·cm^{-2} about 420 mV). CP curve for an electrode with a cell size of 500 µm prepared with laser power of 100 W is much noisier than all the others, which might suggest problems with removing the gas bubbles formed during the reaction. Electrodes with larger cell sizes have poorer performance and the differences between the individual electrodes are visible, with highest activity in the electrodes with the smallest strut diameter, followed by the electrodes with the largest strut diameter and the highest number of particles attached to the surface. Additionally, the performance of all electrodes is slightly decreasing during 1 h CP measurement. Next, a set of electrocatalysts was chosen to be deposited on the surface of all lattice electrodes. For the experimental investigation, two catalysts for OER and two catalysts for HER were selected, which contain a limited amount of noble metals and differ in the number of elements in the material system from binary to quinary. The

composition of the electrocatalyst was chosen based on the literature and electrocatalyst screening studies carried out in our laboratories. As OER electrocatalyst, Ni-Fe (nominal composition: $Ni_{92}Fe_8$) [54] and Cantor alloy ($Co_8Cr_{48}Fe_{11}Mn_{17}Ni_{16}$) [55] material systems were chosen. For HER Pd-Cr-Cu-Ru ($Pd_{40}Cr_7Cu_{25}Ru_{28}$) and Cantor alloy-based systems ($Co_{20}Cr_{20}Fe_{20}Mo_{20}Ni_{20}$) [56] were chosen. Comparisons of the CP curves obtained with each lattice electrode type coated with all mentioned catalysts are presented in Figures 12 and 13. Surprisingly, well known as a good catalyst Ni-Fe (green line in Figure 12) significantly decreased the activity of half of the tested electrodes. For electrodes with 500 µm cell size an increase in performance was observed for the electrodes with the largest pore size and volume (100 W, 100 µs).
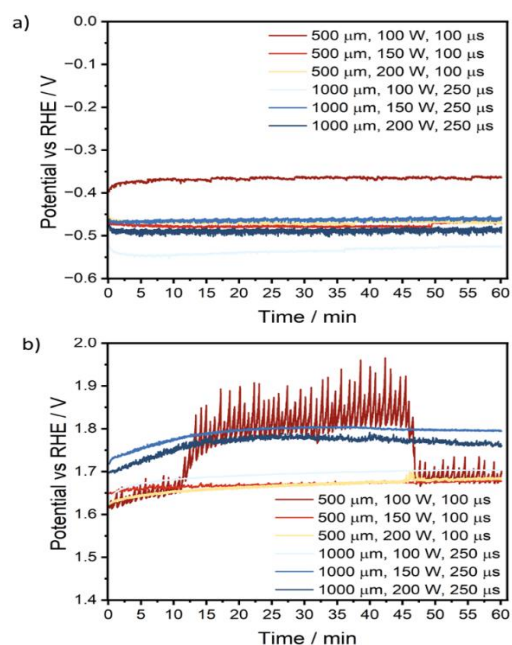

Figure 11: Chronopotentiometry curves recorded for all types of lattice electrodes used as cathodes (a) and anodes (b). Measurements were conducted in 1 M KOH at a current density of -50 mA·cm^{-2} (b) and 50 mA·cm^{-2} (b).

In contrast to electrodes with 1000 μm cell size, electrodes with smaller pore sizes and volumes (150 W, 250 μs and 200 W, 250 μs) showed higher performance. Moreover, the overpotential for OER for all electrodes with Ni-Fe is increasing during the CP measurements, suggesting possible detachment of the coating or maybe selective removal of some elements from the catalyst layer or electrode material itself, but this was not in the scope of this manuscript and was not examined further. As can be seen in Figure 12, the activity trend of Ni-Fe covered electrodes is similar to that of the blank electrodes, with electrodes of smaller unit cell size showing lower overpotentials for OER. On the other hand, deposition of Co-Cr-Fe-Mn-Ni electrocatalyst (pink line in Figure 12) on the surface of electrodes significantly increased the activity for OER, no matter the size of the cell or strut diameter. Furthermore, the stability of the electrodes was good as potential is not significantly changed during CP measurement. The highest improvement in activity was observed for electrodes with 1000 μm cell size prepared with 150 W laser power. The overpotential was decreased by approximately 0.3 V at 50 mA·cm^{-2} compared to the blank electrode.

In the case of catalyst for HER, the experimental results show a clear trend. Both catalysts increase the activity
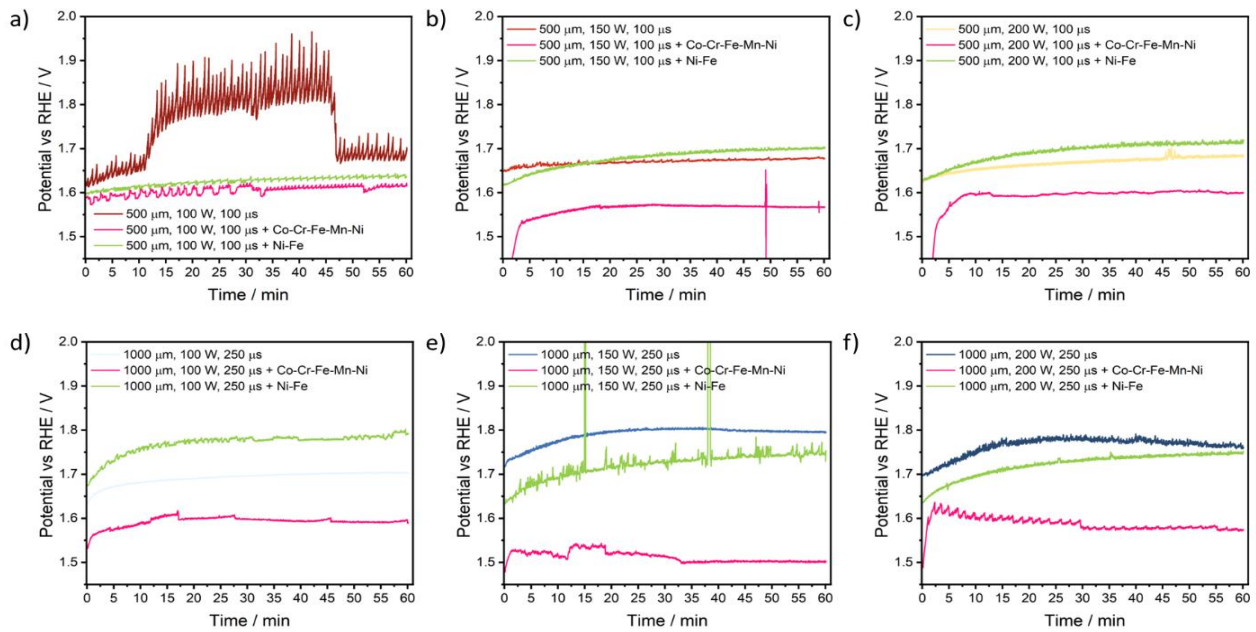

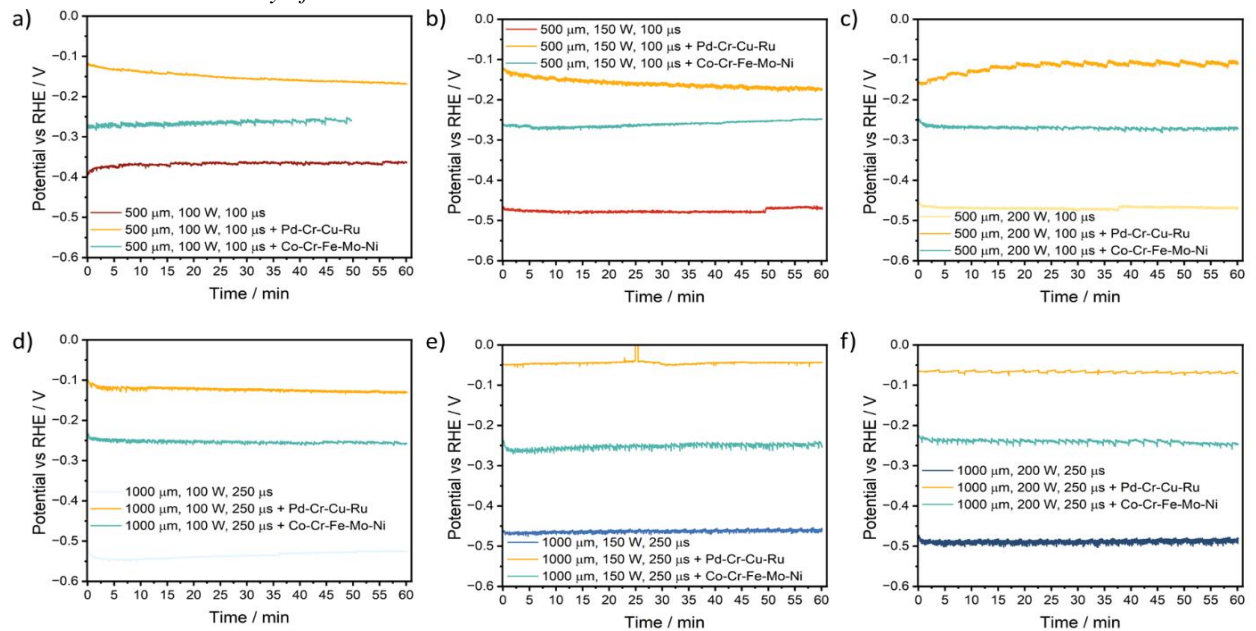*Figure 12. Chronopotentiometry curves recorded for all types of lattice electrodes used as anodes without and with coating with a chosen catalyst: Co-Cr-Fe-Mn-Ni (pink line) and Ni-Fe (green line). Measurements were conducted in 1 M KOH at a current density of 50 mA·cm^{-2}*

Figure 13. Chronopotentiometry curves recorded for all types of lattice electrodes used as cathodes without and with coating with a chosen catalyst: Pd-Cr-Cu-Ru (orange line) and Co-Cr-Fe-Mo-Ni (turquoise line). Measurements were conducted in 1 M KOH at a current density of -50 mA·cm^{-2}
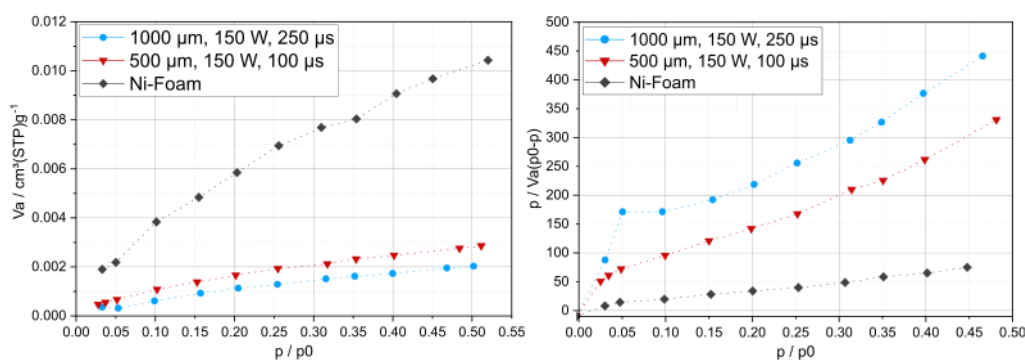
Figure 14: Krypton adsorption (BET) results of lattices and Ni-Foam. Adsorbed volume (left) and BET plot (right)

of all blank electrodes, and the activity of electrodes with Pd-Cr-Cu-Ru is superior compared to those coated with Co-Cr-Fe-Mo-Ni. This trend is in line with expectations as the higher performing catalyst contains two noble metals that are to be good HER catalysts. [57–60] The strongest decrease in overpotential for HER was observed for electrodes with 1000 µm cell size produced with 100 W laser power, followed by electrodes produced with 150 and 200 W laser power. The lowest overpotential for HER, approx. 0.05 V at -50 mA·cm^{-2}, of all electrodes covered with both catalysts was obtained for the electrode with 1000 µm cell size, which was produced with 150 W laser power. The performance of electrodes with smaller cell sizes with Pd-Cr-Cu-Ru was not stable during the measurement period, which is different for electrodes with larger cell sizes. All electrodes with deposited Co-Cr-Fe-Mo-Ni exhibit similar overpotentials for HER and excellent stability during 1 h measurement.

For both reactions, OER and HER, the lowest overpotentials were obtained for the same electrode design with a cell size of 1000 µm and moderate strut diameter and number of attached particles. For OER, Co-Cr-Fe-Mn-Ni and for HER, Pd-Cr-Cu-Ru turned out to be the best electrocatalytic layers. These two electrodes were then analysed with SEM-EDX (Figures 15 and 16). In both cases, the lattice electrode substrate is completely covered with a uniform electrocatalyst layer. The layer is rough with many cracks, which do not reach the basic electrode surface. Also, small particles attached to the strut are fully covered with the catalyst's layers. The Pd-Cr-Cu-Ru layer looks rougher and more finely structured than the Co-Cr-Fe-Mn-Ni layer, but at higher magnification it is observed that the surface of the apparently smooth blocks of Co-Cr-Fe-Mn-Ni consists of a layer of nanoparticles. The morphology of the deposited film did not change during the measurements, which indicates good adhesion and mechanical stability of the deposited layers.
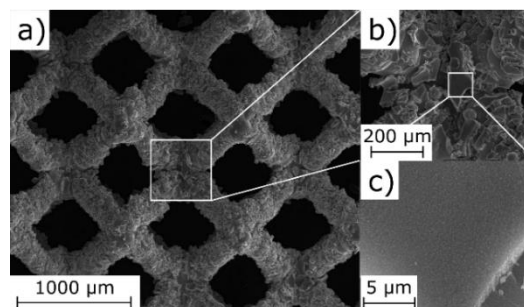

Figure 15: SEM images of a $Co_8Cr_{48}Fe_{11}Mn_{17}Ni_{16}$ coating for oxygen evolution reaction acquired at a magnification of 100x (a), 500x (b) and 20000x (c)
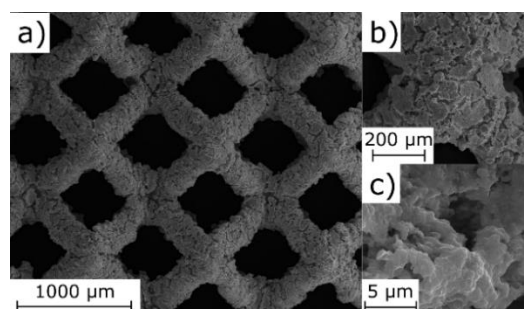

Figure 16: SEM images of a $Pd_{40}Cr_7Cu_{25}Ru_{28}$ coating for hydrogen evolution reaction acquired at a magnification of 100x (a), 500x (b) and 20000x (c)

To provide a further understanding of the coating behaviour, promising uncoated lattice with 1000 µm cell size manufactured with 150 W, a nickel foam counter electrode and a lattice with a cell size of 500 µm lattice manufactured with 150 W are additionally investigated related to the specific surface (see Fig. 14). The BET measurements show an increased specific surface area of 0.0377 m^2·g^{-1} for the nickel foam compared to the lattices with a specific surface area of 0.0072 m^2·g^{-1} (1000um) and 0.0103 m^2·g^{-1} (500um). This is consistent with the observations of powder adhesion and strut diameter, as a smaller strut diameter increases the specific surface area.

4. Conclusion and outlook

In this study, lattices with a unit cell size of 250 μm, 500 μm and 1000 μm were manufactured from NiCr19Fe19Nb5Mo3 using a spot-based exposure strategy and the influence of the process parameters on the fabricated structures was evaluated. The evaluation results show that the strut diameter increases for lattices manufactured with increasing energy, with more powder particles being attached to the fabricated structure due to a smaller focal diameter and higher laser power, which is considered beneficial. Based on a selection of promising process parameters, lattices with a unit cell size of 500 μm and 1000 μm were coated using $Ni_{92}Fe_8$ and $Co_8Cr_{48}Fe_{11}Mn_{17}Ni_{16}$ (OER) and $Pd_{40}Cr_7Cu_{25}Ru_{28}$ and $Co_{20}Cr_{20}Fe_{20}Mo_{20}Ni_{20}$ (HER), respectively. Investigation of electrocatalytic performance was performed using a lab-scale three-electrode flow-through cell. Comparing chronopotentiometry curves recorded on the electrodes with catalyst layers deposited on them revealed that for both oxygen and hydrogen evolution reactions, the lowest overpotential was obtained for the electrode with 1000 μm cell size prepared with 150 W laser power. Therefore, this electrode design is considered favourable for the application in a flow-through water electrolyser. Additionally, overpotentials obtained for HER and OER by the electrode with this design coated with $Pd_{40}Cr_7Cu_{25}Ru_{28}$ (50 mV at -50 mA·cm^{-2}) and $Co_8Cr_{48}Fe_{11}Mn_{17}Ni_{16}$ (270 mV at 50 mA·cm^{-2}), respectively, are close to the overpotentials recorded for state-of-the-art catalyst reported in the literature which makes those initial results worth further investigation [61, 62]. Future research will aim to investigate the scalability and exploitation of design freedom of additive manufacturing for the design of new electrodes.

5. Acknowledgement

References

1. IEA, International Energy Agency Net Zero by 2050 - A Roadmap for the Global Energy Sector
2. Allwood et al. (2010): Options for achieving a 50% cut in ind. carbon emissions by 2050. Env. Sc. & T. 44:1888–1894. https://doi.org/10.1021/es902909k
3. Oliveira et al. (2021) A green hydrogen economy for a ren. en. soc. Curr. Op. in Chem. Eng. 33:100701. https://doi.org/10.1016/j.coche.2021.100701
4. Alzoubi (2021) Renewable Green hydrogen energy impact on sustainability performance. Int J CIM 1. https://doi.org/10.54489/ijcim.v1i1.46
5. O'Dwyer et al. (2022) Long-Term Hydrogen Storage - A Case Study Exploring Pathways and Investments. Energies 15:869. https://doi.org/10.3390/en15030869
6. Zhang et al. (2018) Progress in nanostructured (Fe or Co)/N/C non-noble metal electrocatalysts for fuel cell oxygen reduction reaction. Electrochimica Acta 262:326–336. https://doi.org/10.1016/j.electacta.2018.01.046
7. DIN e.V. (2018) Additive Fertigung - Grundlagen - Terminologie (ISO/ASTM DIS 52900:2018)
8. Gebhardt (2017) Additive Fertigungsverfahren: Add. Man. und 3D-Dr. für Prototyping - Tooling – Produktion. Hanser Verlag, München
9. VDI (2014) Additive Fertigungsverfahren - Grundlagen, Begriffe, Verfahrensbeschreibungen (3405)
10. Chen et al. (2021) Additive manufacturing of metallic lattice structures: Unconstrained design, accurate fabrication, fascinated performances, and challenges. Materials Science and Engineering: R: Reports 146:100648. https://doi.org/10.1016/j.mser.2021.100648
11. Nagesha et al. (2020) Rev. on char. and impacts of the lattice structure in add. Man. Mat. Tod.: Proc. 21:916–919.
12. Hussein et al. (2013) Advanced lattice support structures for metal add. man. J. of M. Proc. T.213:1019–1026.
13. Muñoz et al. (2022) Design of bimetallic 3D-printed electrocatalysts via galvanic replacement to enhance en. conv. systems. App. Cat. B: Environmental 316:121609.
14. Boursier et al. (2022) Exp. and Num. Investigation of a Lattice Structure for Energy Absorption: Application to the Design of an Aut. Crash Abs. Polymers 14:1116.
15. Seharing et al. (2020) A review on integration of lightweight gradient lattice structures in add. man. parts. Adv. in Mech. Eng. 12:168781402091695.
16. Tang et al. (2018) Lattice Structure Design and Optimization with Additive Manufacturing Constraints. IEEE Trans Automat Sci Eng 15:1546–1562.
17. Uribe-Lam et al. (2021) Use of additive manufacturing for the fabrication of cellular and lattice materials: a review. Materials and Manufacturing Processes 36:257–280. https://doi.org/10.1080/10426914.2020.1819544
18. Liu et al. (2022) Prog. of Porous/Lattice Structures App. in Thermal Man. Tech. of Aerospace App. Aerospace 9:827. https://doi.org/10.3390/aerospace9120827
19. Mojabi et al. (2023) Additive manufacturing: New paradigm for developing water splitting systems. International Journal of Hydrogen Energy.
20. dos Santos et al. (2019) Ni−Fe (Oxy)hydroxide Modified Graphene Additive Manufactured (3D-Printed)

Electrochemical Platforms as an Efficient Electrocatalyst for the Oxygen Evolution Reaction. ChemElectroChem 6:5633–5641. https://doi.org/10.1002/celc.201901541

21. Hüner et al. (2023) Ni-Pt coating on graphene based 3D pr. el. for hydrogen ev. reactions in alk. media. Fuel 331:125971. https://doi.org/10.1016/j.fuel.2022.125971

22. Hüner et al. (2022) Electrodeposition of NiCu bimetal on 3D pr. electrodes for hydrogen ev. reactions in alk. media. Int. J. of Hydr. En. 47:12136–12146.

23. Gusmão et al. (2019) MoS2 versatile spray-coating of 3D electrodes for the hydrogen ev. reaction. Nanoscale 11:9888–9895. https://doi.org/10.1039/C9NR01876J

24. Novčić et al. (2021) Local electrochemical activity of transition metal dichalcogenides and their heterojunctions on 3D-printed nanocarbon surfaces. Nanoscale 13:5324–5332. https://doi.org/10.1039/D0NR06679F

25. Ahn et al. (2022) 3D-printed NiFe-layered double hydroxide pyramid electrodes for enh. electrocatalytic oxygen evolution reaction. Sci Rep 12:346.

26. Zhang et al. (2022) AM 3D customizable low-cost superwetting polyacrylate-based hierarchically micro-nanoporous lattice anode for energy-saving large-current-density water splitting application. Comp. Part B: Eng. 245:110189. doi.org/10.1016/j.compositesb.2022.110189

27. Han et al. (2022) Direct photo-curing 3D printing of nickel-based electrocatalysts for highly-efficient hydrogen evolution. Nano Energy 102:107615.

28. Lodhi et al. (2019) Additively manufactured 316L stainless steel: An efficient electrocatalyst. International Journal of Hydrogen Energy 44:24698–24704.

29. Ambrosi et al. (2016) Helical 3D-Printed Metal Electrodes as Custom-Shaped 3D Platform for Electrochemical Devices. Adv. Funct. Mat. 26:698–703.

30. Guo et al. (2022) 3D Printing of Multiscale Ti64-Based Lattice Electrocatalysts for Robust Oxygen Evolution Reaction. Advanced Science 9:e2201751.

31. Cai HY, Ma JF, Li NN et al. (2022) Inv. on hydrogen ev. reaction performance of porous electrode prepared by laser powder bed fusion. Ren. En. 185:771–778.

32. Ambrosi & Pumera (2018) Multimaterial 3D-Printed Water Electrolyzer with Earth-Abundant Electrodeposited Catalysts. ACS Sustainable Chem Eng 6:16968–16975.

33. Ambrosi & Pumera (2018) Self-Contained Polymer/Metal 3D pr. Electrochem. Platform for Tailored Water Splitting. Adv Funct. Mat. 28. doi.org/10.1002/adfm.201700655

34. Zhou et al. (2022) Corrosion engineering boosting bulk Fe50Mn30Co10Cr10 high-entropy alloy as high-efficient alkaline ox. Ev. reaction electroc. Journal of Mat. Sc. & Tec. 109:267–275. doi.org/10.1016/j.jmst.2021.09.003

35. Löffler et al. (2021) What Makes High-Entropy Alloys Exceptional Electrocatalysts? Ang. Chem. Int. Ed. 60:26894–26903. https://doi.org/10.1002/anie.202109212

36. Wang et al. (2022) Recent Progress in High Entropy Alloys for Electrocatalysts. Electrochem Energy Rev 5:1–28. https://doi.org/10.1007/s41918-022-00144-8

37. Zhang et al. (2022) Recent research progress on high-entr. alloys as electrocat. mat. J. of All. & Comp.918:165585.

38. Cai et al. (2021) Nanoporous ultra-high-entr. All. Cont. 14 el. for wat. splitting electrocat. Chem. Sc. 12.

39. Broge et al. (2023) Facile Solvothermal Synthesis of Pt–Ir–Pd–Rh–Ru–Cu–Ni–Co High-Entropy Alloy Nanoparticles. Chemistry of Materials 35:144–153.

40. Modeshia & Walton (2010) Solvothermal synthesis of perovskites and pyrochlores: crystallisation of functional oxides under mild conditions. Chemical Society Reviews 39:4303–4325. https://doi.org/10.1039/B904702F

41. Knorpp et al. (2022) Hydrothermal synthesis of multi-cationic high-entropy layered double hydroxides. RSC Adv. 12. https://doi.org/10.1039/D2RA05435C

42. Yao et al. (2018) Carbothermal shock synthesis of high-entropy-alloy nanoparticles. Science 359:1489–1494.

43. Biesuz et al. (2021) Solidification microstructures of multielement carbides in the high entropy Zr-Nb-Hf-Ta-Cx system produced by arc melting. Scr. Mat. 203:114091. https://doi.org/10.1016/j.scriptamat.2021.114091

44. Arif et al. (2022) Laser deposition of high-entropy alloys: A comprehensive review. Optics & Laser Technology 145:107447. doi.org/10.1016/j.optlastec.2021.107447

45. Sreeramagiri et al. (2022) Comparison of laser deposition methods for the synthesis of AlxCoCrFeNi multi-principal element alloy. J. of Mat. Res. & Tech. 19:1090–1101.

46. Batchelor et al. (2021) Complex-Solid-Solution Electrocatalyst Discovery by Computational Prediction and High-Throughput Experimentation. Ang. Chem. Int. Ed. 60:6932–6937. doi.org/10.1002/anie.202014374

47. Tsai et al. (2015) Oxidation resistance and characterization of (AlCrMoTaTi)-Six-N coating deposited via magnetron sputtering. Journal of Alloys and Compounds 647:179–188. https://doi.org/10.1016/j.jallcom.2015.06.025

48. Zhou et al. (2022) Chemical vapor deposition diamond nucleation and initial growth on TiZrHfNb and TiZrHfNbTa high entropy alloys. Materials Letters 309:131366. doi.org/10.1016/j.matlet.2021.131366

49. Shojaei et al. (2022) Rev. of electrode. Meth. for the preparation of high-entropy alloys. Int J Min. Met. Mat. 29:1683–1696. doi.org/10.1007/s12613-022-2439-y

50. Yang et al. (2020) Aerosol Synthesis of High Entropy Alloy Nanoparticles. Langmuir 36:1985–1992.

51. Cechanaviciute et al. (2022) Aerosol-Based Synthesis of Multi-metal Electrocatalysts for Oxygen Evolution and Glycerol Oxidation. ChemElectroChem 9:e202200107.

52. Cechanaviciute et al. (2023) Scalable Synthesis of Multi-Metal Electrocatalyst Powders and Electrodes and their Application for Oxygen Evolution and Water Splitting. Ang. Chem. Int. Ed. Chemie International Edition 62:e202218493. https://doi.org/10.1002/anie.202218493

53. Erpro group Material data sheet IN718/2.4668

54. Xiao et al. (2018) Synergy between Fe and Ni in the optimal performance of (Ni,Fe)OOH catalysts for the oxygen evolution reaction. Proc Natl Acad Sci U S A 115:5872–5877. doi.org/10.1073/pnas.1722034115

55. Strotkötter et al. (2022) Discovery of High-Entropy Oxide Electrocat.: From Thin-Film Material Libraries to Particles. Chem. Mat. Mater 34:10291–10303. doi.org/10.1021/acs.chemmater.2c01455

56. Schumacher et al. (2022) High-throughput discovery of hydrogen evolution electroc. in the css system Co–Cr–Fe–Mo–Ni. J Mater Chem A 10:9981–9987.

57. Bae et al. (2020) Recent advances in ruthenium-based electrocatalysts for the hydrogen evolution reaction. Nan. Horiz 5:43–56. https://doi.org/10.1039/C9NH00485H

58. Luo et al. (2020) Ru-based electrocatalysts for hydrogen evolution reaction: Recent research advances and perspectives. Mat. Tod. Phy. 15:100274.

59. Sarkar & Peter (2018) An overview on Pd-based electrocatalysts for the hydrogen evolution reaction. Inorg Chem Fr. 5:2060–2080. doi.org/10.1039/C8QI00042E

60. Zhang et al. (2016) Recent advances in palladium-based electroca. for fuel cell reactions and hyrd. Ev. React. Nano En. 29:198–219. doi.org/10.1016/j.nanoen.2016.02.044

61. Vesborg et al. (2015). Recent development in hydrogen evolution reaction catalysts and their practical impl. The journal of phys. Chem. letters, 6(6), 951-957.

62. Xie et al. (2022). Oxygen evolution reaction in alkaline environment: material challenges and solutions. Advanced Functional Materials, 32(21), 2110036.